



**A SCALABLE MASS CUSTOMISATION DESIGN PROCESS FOR
3D-PRINTED RESPIRATOR MASK TO COMBAT COVID-19**

Journal:	<i>Rapid Prototyping Journal</i>
Manuscript ID	RPJ-10-2020-0231.R2
Manuscript Type:	Original Article
Keywords:	COVID-19, Face mask, Design automation, Custom fit, Additive Manufacturing, Mass Customisation

SCHOLARONE™
Manuscripts

1 A SCALABLE MASS CUSTOMISATION DESIGN PROCESS FOR 3D-PRINTED 2 RESPIRATOR MASK TO COMBAT COVID-19

3 4 **Abstract:**

5 **Purpose:** 3D printed custom-fit respirator mask has been proposed as a promising solution to
6 alleviate mask-related injuries and supply shortage during COVID-19. However, creating a
7 custom-fit CAD model for each mask is currently a manual process and thereby not scalable
8 for a pandemic crisis. This paper aims to develop a novel design process to reduce overall
9 design cost and time, thus enabling the mass customisation of 3D printed respirator masks.

10 **Methodology:** Four data acquisition methods were employed to collect 3D facial data from
11 five volunteers. Geometric accuracy, equipment cost and acquisition time of each method were
12 evaluated to identify the most suitable acquisition method for a pandemic crisis. Subsequently,
13 a novel three-step design process was developed and scripted to generate respirator mask CAD
14 models for each volunteer. Computational time was evaluated and geometric accuracy of the
15 masks were evaluated via one-sided Hausdorff distance.

16 **Findings:** Respirator masks were successfully generated from all meshes, taking <2
17 minutes/mask for meshes of 50,000~100,000 vertices, and <4 minutes for meshes of ~500,000
18 vertices. The average geometric accuracy of the mask ranged from 0.3 mm to 1.35 mm,
19 depending on acquisition method. The average geometric accuracy of mesh obtained from
20 different acquisition methods ranged from 0.56 mm to 1.35 mm. A smart phone with a depth
21 sensor was found to be the most appropriate acquisition method.

22 **Originality:** A novel and scalable mass customisation design process was presented, which can
23 automatically generate CAD models of custom-fit respirator masks in a few minutes from a
24 raw 3D facial mesh. Four acquisition methods, including the use of a statistical shape model, a
25 smart phone with a depth sensor, a Light Stage, and a structured light scanner were compared;
26 one method was recommended for use in a pandemic crisis considering equipment cost,
27 acquisition time and geometric accuracy.

28 **Practical implications:** The proposed process can be adapted for other types of facial PPE
29 and wearables.

30 **Keywords:** COVID-19, Face mask, Design automation, Custom fit, Mass Customisation,
31 Additive Manufacturing

1
2
3 1 **Article Classification:** Research paper
4
5
6 2

7
8 3 **1. Introduction**
9

10 4 In June, the World Health Organisation (WHO) affirmed the transmission of COVID-19 by
11 5 asymptomatic or pre-symptomatic individuals based on growing evidence (WHO, 2020), health
12 6 agencies worldwide have begun to adopt a change in stance to embracing a policy of
13 7 encouraging or enforcing mask-wearing. This has created a huge strain on the global supply of
14 8 respirator masks to frontline Healthcare Personnel (HCP) who are continuously faced with high
15 9 patient numbers and the threat of infection. Increasingly, reusable respirators (e.g. elastomeric
16 10 half-mask respirator commonly used in construction and manufacturing) have been proposed
17 11 as an alternative to disposable respirators (e.g. FFP3 or N95) in a pandemic situation to address
18 12 the problem of supply shortages (Pompeii et al., 2020). However, regardless of reusable or
19 13 disposal respirators, studies have shown significant failure rates for mask-fitting of HCP
20 14 ranging from 9.8% to 54%, largely attributable to a high variance of facial characteristics
21 15 arising from demographic differences (Wilkinson et al., 2010, Yu et al., 2014). A previous
22 16 respirator fit test study (n=6,160) has shown strong associations between the race of participants
23 17 and differences in facial features, which resulted in statistically significant differences in fit test
24 18 failure rates (Wilkinson et al., 2010). Hospitals with a multi-racial HCP population makeup can
25 19 be particularly susceptible towards high fit test failure rates, thereby compromising on the
26 20 availability of frontline deployable workforce and putting increased strains on the healthcare
27 21 system in a public health emergency, such as the ongoing COVID-19 pandemic.

22 22 Apart from meeting high demands for respirators, it is equally important to ensure good fit
23 23 and comfort for HCP, who often must don respiratory Personal Protective Equipment (PPE)
24 24 for long periods on a regular basis. A recent study reported high incidence (97%) of skin
25 25 damage related to enhanced infection-prevention measures, including prolonged wearing of
26 26 respirators, especially over the nasal bridge and cheeks (Lan et al., 2020). High pressure at the
27 27 skin/mask interface and long duration of mask wearing has been identified as key risk factors
28 28 responsible for device-related pressure ulcers (Gefen et al., 2020). Such occupational hazards
29 29 can put frontline HCP at greater risks of infection, undermine efficiencies and lead to loss of
30 30 precious manpower in a pandemic. Custom fitting respirator masks to HCP would significantly
31 31 reduce fit-failure rates, occurrences of skin damage and increase HCP comfort.

1
2
3 1 Since the start of the COVID-19 pandemic, 3D printing has been utilized by makers,
4 2 communities and institutions in various places to produce PPE locally to combat supply chain
5 3 shortage (Novak and Loy, 2020a, Novak and Loy, 2020b, Wesemann et al., 2020). Various
6 4 papers have been published to review and evaluate existing 3D printed PPE designs (Wesemann
7 5 et al., 2020, Novak and Loy, 2020a, Novak and Loy, 2020b, Flanagan and Ballard, 2020,
8 6 Clifton et al., 2020), and many introduced methods of PPE design and production, such as
9 7 connectors for breathing devices (Cavallo et al., 2020, Greig et al., 2020), face shields
10 8 (Flanagan and Ballard, 2020, Celik et al., 2020), and re-usable respirators (Provenzano et al.,
11 9 2020, Greig et al., 2020, Swennen et al., 2020). These papers demonstrated the advantages of
12 10 3D printing in combating local supply chain shortage, and also pointed out limitations in the
13 11 areas of design, manufacture and regulations to provide valuable insights for future 3D printed
14 12 PPE design and production. However, a major benefit of 3D printing PPE was often
15 13 overlooked; the ability to produce designs tailored to each individual, thus missing the potential
16 14 to produce PPE with better fit and comfort for HCP. As supply chain gradually stabilises
17 15 through the middle of 2020, it is important for us to look ahead and develop novel design
18 16 strategies that can maximize the advantages of 3D printing to combat the long-term threat of
19 17 COVID-19 and future health crises (Gates, 2020).

20
21
22 18 To date the key strategy employed for the design of PPE has been modularisation enabled
23 19 by anthropometric sizing (classifying the anthropometric characteristics of a population into a
24 20 few represented groups) (Hsiao, 2013). Modularisation does enable manufacturers to employ
25 21 mass-production technology to offer products at minimal unit cost. However, modularisation
26 22 does not enable true customisation for each individual, instead only a small amount of product
27 23 variation is created. Some individuals will lie outside of the sizing archetypes, as demonstrated
28 24 by fit-test failure rates. As populations become increasingly biologically admixed due to
29 25 globalisation, regular studies need be carried out to form accurately representative statistical
30 26 models that reflect the composition changes in a population, making this method time
31 27 consuming, labour intensive and economically prohibitive.

32
33
34 28 The existing limitations for customisation in modularised designs can be avoided with the
35 29 use of 3D printing or Additive Manufacture (AM), which has negligible tooling costs associated
36 30 with producing one-off items. This makes AM a cheaper alternative for the Mass Customisation
37 31 (MC) of products as compared to existing mass-production technologies (e.g. injection
38 32 moulding), as large costs incurred to alter any tools, moulds, processes due to product design

1 changes for each individual can now be minimised. Therefore, designers and companies can
2 avoid employing anthropometric sizing-based design methodologies and move towards new
3 mass-customisation methods. However, while AM creates a manufacturing route for
4 customised products and the associated costs are likely to fall as the technology matures; a key
5 barrier repeatedly noted in literature is a recursive labour-intensive design process to create
6 Computer-Aided Design (CAD) models for each individual (Rogers et al., 2007, Pallari et al.,
7 2010, Tuck et al., 2008, Salles and Gyi, 2012). Previous studies focused on demonstrating the
8 feasibility of using AM technologies and comparing their performance with those fabricated
9 through craft production (Rogers et al., 2007, Paterson et al., 2014, Schrank, 2011, Pallari et
10 al., 2010) or mass production (Cheng and Chu, 2013, Salles and Gyi, 2013a, Salles and Gyi,
11 2013b, Tuck et al., 2008, Salles and Gyi, 2012). Swennen et. al. (Swennen et al., 2020)
12 proposed using 3D printing to produce customised respirator masks when FFP2/3 masks are
13 not available in a pandemic. However, the employed design process was predominantly manual
14 and required expert knowledge in data acquisition (collect the body shape of an individual via
15 a 3D scanning device), data manipulation (extract useful anthropometric data) and CAD
16 modelling (adapt the geometry of a CAD model to the extracted anthropometric data). Salles
17 and Gyi noted that the cost for employing a CAD specialist to create engineering drawings of
18 custom-fit shoe insoles was the second highest among all costs, with fabrication cost being the
19 first (Salles and Gyi, 2013a, Salles and Gyi, 2012). Studies have also shown that time taken
20 from obtaining anthropometric 3-dimensional (3D) data to the creation of a single custom-fit
21 CAD model in a manual design process can amount to approximately 20 - 30% of the overall
22 production time (Salles and Gyi, 2013a, Tuck et al., 2008, Salles and Gyi, 2012). This labour-
23 intensive and knowledge-driven design process adds unit cost and time to production, and
24 therefore, in many instances makes MC economically unviable. To reduce the design process
25 cost, labour wages could be lowered, but this appears unsustainable and intellectually
26 unstimulating. Apart from cost, slight variations and errors may be introduced during a manual
27 design process (Spallek and Krause, 2016), which will undermine the reproducibility of design
28 features and thereby its intended functionalities. Alternatively, the development of smart
29 processes to minimise manual interaction in a design process is an attractive option.

30 Significant advances have been made over the years to automate or simplify parts of the
31 custom-fit design process. In recent years, statistical shape models of heads and faces have been
32 used to predict 3D head and facial shapes from 1D anthropometric measurements, thereby
33 removing the need of 3D scanners in the data acquisition step (Verwulgen et al., 2018, Lacko

1
2
3 1 et al., 2017, Chu et al., 2017, Chu et al., 2015). Advances in 3D scanning technologies have
4 2 also brought about affordable handheld 3D scanners to make the acquisition process less
5 3 cumbersome. However, the trade-offs between accuracies, time and costs across different data
6 4 acquisition methods, including the use of a statistical shape model, has not been evaluated
7 5 before. Significant advances have also been made for the CAD modelling step, particularly for
8 6 medical device applications such as custom-fit hearing aids (Unal et al., 2008), splints and
9 7 orthoses (Schrank, 2011, Paterson et al., 2014, Cazon et al., 2014). Most of these studies made
10 8 use of Application Programming Interface (API) in commercial CAD packages to achieve
11 9 automatic creation and modification of a CAD model by adjusting the values of a few
12 10 parameters (e.g. dimensions) that define the model. APIs have been widely recognised as a key
13 11 enabler of MC due to its flexibility in design modification (Fogliatto et al., 2012, Da Silveira
14 12 et al., 2001). While these studies provided user-friendly co-design platforms to de-skill the
15 13 CAD modelling process for non-engineering communities (e.g. medical community) and
16 14 supported the increasing commercialisation of automated processes in certain industries, these
17 15 processes can still take up to half an hour to create a single design as medical practitioners need
18 16 to manually manipulate the raw scan and incorporate their clinical knowledge during the design
19 17 process to ensure optimally designed devices for an individual (Cazon et al., 2014). However,
20 18 in a pandemic crisis, the design of a custom-fit respirator mask for a HCP should involve as
21 19 little manual work and time from a HCP as possible to maximize their time for patients and to
22 20 meet demand for a larger population of HCP. To the best of the authors' knowledge, no study
23 21 has demonstrated a scalable MC design strategy for 3D printed respirator masks before.

22 In this paper, we propose a scalable MC design process for a concept respirator mask design
23 for 3D printing. We first evaluated the trade-offs between four acquisition methods by
24 comparing their geometric accuracy, acquisition time and equipment costs to look for an
25 appropriate acquisition method for a pandemic crisis. Then, we investigated the feasibility of
26 automating the data manipulation and CAD modelling steps for creating a concept respirator
27 mask. A novel three-step process has been developed to achieve automation. The process starts
28 with a template fitting step which brings raw facial meshes into dense correspondence.
29 Followed by a data extraction step which uses vertices on the fitted mesh as landmarks to
30 identify and extract a region of interest on the face that the mask will be in contact with. Finally,
31 a parametric CAD modelling step to generate custom-fit CAD model. The process was
32 subsequently converted into scripts written in Fusion 360 API (Autodesk, Inc., USA) and
33 MATLAB (MathWorks, Massachusetts, USA) to achieve automation at each step. Five

1
2
3 1 volunteers were recruited for the evaluation of the acquisition methods and the new design
4
5 2 process.

6 7 8 **2. Method**

9
10 4 Five volunteers with varying age, gender, and ethnicity (summarised in Table I) were recruited
11
12 5 at Imperial College London (UK) in February 2020 following Protocol (19IC5167) approved
13
14 6 by Imperial College Research Ethics Committee. A 4 step process (Figure 1) was employed to
15
16 7 convert data of each volunteer into a custom-fit respirator:

- 17 8 1. Data acquisition; facial geometry of each volunteer in the format of a digital 3D facial
18
19 9 mesh was collected via four acquisition methods. Volunteers were asked to remain in a
20
21 10 natural position and face in a neutral expression with mouth and eyes closed to minimize
22
23 11 variation in results between different acquisition methods for the same volunteer.
- 24 12 2. Template fitting; the shape of a template facial mesh was morphed or fitted to the shape
25
26 13 of the input racial mesh.
- 27 14 3. Region of Interest extraction; topographical data were identified and extracted from the
28
29 15 fitted facial mesh.
- 30 16 4. CAD modelling; a custom-fit respirator mask CAD model was automatically generated
31
32 17 from a Fusion 360 API script.

33 34 35 36 **2.1 Data acquisition**

37
38 19 Four different approaches to acquire 3D facial geometry were employed; one based on
39
40 20 structured light reconstruction, one based on photometric-stereo, one that combines both, and
41
42 21 one based on 3D reconstruction from a single 2-Dimensional (2D) image using a statistical
43
44 22 shape model. With all the above methods, the resulting geometry is represented as a
45
46 23 triangulated mesh. Table II provides a summary of the four acquisition methods, including
47
48 24 details of equipment, software and output file. Figure 2 shows 3D meshes obtained from each
49
50 25 method.

51 26 The first acquisition method is by reconstructing 3D facial geometry from a 2D image
52
53 27 using a morphable model. 3D facial shape reconstruction from a 2D image is an ill-posed
54
55 28 problem, but it is also a well-researched area in computer science as it is an interesting problem
56
57 29 to solve. The seminal work by Blanz and Vetter (Blanz and Vetter, 1999) was the first to
58
59 30 demonstrate that it is possible to synthesise a 3D face from a single 2D image with the use of
60
31 a morphable model which contains a statistical shape model and a statistical texture model.

1
2
3 1 The morphable model provides a shape and a texture space that covers the variation in shape
4 and texture of a group of similar faces. When given a 2D image, it searches through the space
5 2
6 3 to generate a realistic 3D face that best matches the face in that 2D image. In this study, the
7
8 4 publicly available morphable model, Large-scale Statistical Face Model (LSFM) developed by
9
10 5 Booth et al. (Booth et al., 2018) was employed to generate 3D facial meshes. The LSFM was
11
12 6 developed by learning the shape and texture space of 9,663 facial scans captured over a period
13
14 7 of 4 months via a 3dMD™ photometric-stereo capture device. The result of this learning was
15
16 8 a morphable triangular mesh with 53,215 vertices, whose shape can be modified into different
17
18 9 realistic 3D facial shapes with the input of 2D images. For each volunteer, a 2D “in-the-wild”
19
20 10 image (image taken under no constraints in terms of lighting, background etc.) of his/her face
21
22 11 in neutral expression was taken from an Apple Iphone 6s (Apple Inc., Cupertino, California,
23
24 12 USA). This image was then loaded into the LSFM to alter the shape of the morphable mesh to
25
26 13 match as closely as possible the shape and texture of the input image. The output of the LSFM
27
28 14 will follow the mesh structure of the morphable mesh, which is a triangular mesh with 53,215
29
30 15 vertices. An example of the LSFM output mesh is shown in Figure 2 (a).

31
32 16 The second acquisition method is via the use of a Light Stage capturing system for
33
34 17 photometric-stereo reconstruction. Light Stage was first introduced by Debevec (Debevec,
35
36 18 2012) as a reflectance acquisition setup, and it can be used as a high-quality 3D facial geometry
37
38 19 acquisition device (Kampouris et al., 2018, Ghosh et al., 2011, Lattas et al., 2019). It comprises
39
40 20 of a room-spanning sphere, mounted with controllable lights that illuminate a subject and
41
42 21 cameras that capture the subject from different known view-points. The Imperial College
43
44 22 Multispectral Light Stage (Kampouris and Ghosh, 2018) was used in this study. A volunteer
45
46 23 was asked to sit inside the sphere with eyes closed and in neutral expression. Images of the
47
48 24 volunteer’s face were captured in the Light Stage under a uniform illumination and base
49
50 25 geometry of the subject’s face was reconstructed from these images using the state-of-the-art
51
52 26 Structure-from-Motion (SfM) COLMAP photometric-stereo algorithm (Schönberger et al.,
53
54 27 2016, Schonberger and Frahm, 2016). A universal template (mean shape) created from the
55
56 28 LSFM study was employed to align the reconstructed meshes: a landmark localisation method
57
58 29 (Sagonas et al., 2013) was employed to automatically landmark 2D images rendered from the
59
60 30 reconstructed mesh and projected 3D landmarks back into the reconstructed mesh; then rigidly
31
32 31 align the reconstructed mesh to the mean shape of LSFM by calculating the transformation
33
34 32 matrix using their respective facial landmarks. Finally, as the reconstructed mesh was in an
35
36 33 arbitrary topology, the method of quadratic edge collapse decimation from MeshLab

1
2
3 1 (MeshLab, 2020) was employed to reduce the mesh to about 50,000 vertices. All final meshes
4 are triangular mesh (Figure 2b) with an average file size of 5MB.
5
6
7

8 3 The third acquisition method combines structured light and RGB input, which are captured
9 as an RGB + Depth video sequence from the TrueDepth camera in Apple Iphone X (Apple Inc.,
10 Cupertino, California, USA). It works by projecting a dotted infrared light pattern of 30,000
11 dots on a face while capturing their reflection. Bellus3D app (*Face mode*) was used for aligning
12 captured frames and for merging the depth and RGB captures from each image into a single 3D
13 triangular mesh. During capture, the volunteer is asked to hold the Iphone X in front of his face
14 and turn his head from side to side, while maintaining a neutral expression with mouth closed.
15 The mesh was then exported in *HD resolution* from the app. The resulting mesh (Figure 2c)
16 has an average size of 10MB, containing about 100,000 vertices. Also, in contrast with the
17 previous methods, it does not require the attendance of a scanning expert.
18
19
20
21
22
23
24
25

26 13 The fourth acquisition method is via the use of a structured-light based capturing system,
27 Artec Space Spider from Artec 3D (Artec 3D, Luxembourg). It is a handheld 3D scanner that
28 works by projecting pulsed blue light onto a person's face. As reported by the manufacturer, it
29 has a 3D resolution up to 0.1mm and 3D point accuracy up to 0.05 mm. During data acquisition,
30 a volunteer was seated on a movable chair with eyes and mouth closed, head in a natural
31 position and face in a neutral expression, while an experienced technician moved the scanner
32 from one side of the face to another in a steady pace to capture the entire face. Artec Studio 11
33 Professional software was used to receive and process data transmitted from the scanner and
34 create 3D meshes. The average file size of one mesh is over 50MB, containing over 500,000
35 vertices, [as shown in Figure 2 \(d\)](#).
36
37
38
39
40
41
42
43

44 23 **2.2 Template fitting**

45
46 24 Once a scanned 3D facial mesh was obtained, it was fitted to a universal template facial mesh.
47 This is a crucial step to remove heterogeneity across different raw facial meshes in terms of
48 orientation, location, and mesh structure (vertex indexing and triangulation), thereby enabling
49 the subsequent automatic extraction of topographical data from a large facial dataset. In this
50 study, the template mesh used is the mean shape created from the LSFM. It is made of 53,215
51 vertices indexed in an orderly fashion in a regular triangular mesh structure, as shown in Figure
52 3. An algorithm was developed in MATLAB to achieve template fitting in a four-stage process:
53
54
55
56
57
58
59
60

1
2
3 1 pre-processing, coarse rigid alignment, fine rigid alignment, and non-rigid alignment stage.
4
5 2 These stages are highlighted in Figure 4 (a). Details of the algorithm are explained as follows.
6
7

8 3 The first operation in the pre-processing stage is to match the scale of the raw mesh to the
9
10 4 template mesh by comparing the order of magnitude of each axes range. Once the mesh is
11
12 5 scaled correctly, the vertices of the raw mesh are checked through to find the minimum values
13
14 6 in x -, y -, and z -axis directions and compared with those of the template. The differences in the
15
16 7 minimum values in each axis were used to translate the raw mesh to a position relatively close
17
18 8 to the template mesh. Next, at the coarse alignment stage, an error minimization technique was
19
20 9 employed to determine a rotation matrix which re-orientates the raw mesh to the same plane
21
22 10 as that of the template mesh. 2D outlines of the raw mesh and the template mesh were projected
23
24 11 onto the X-Y, X-Z, and Y-Z planes as shown in Figure 4 (b). Then, the raw mesh was
25
26 12 incrementally rotated along the X, Y, and Z axis through its centroid while the area of
27
28 13 overlapping between the raw mesh and the template mesh, as well as the area falling outside
29
30 14 of the template mesh, were calculated. The rotation matrix that gave the maximum overlapping
31
32 15 area and minimum area falling outside of the template mesh was used to perform rigid
33
34 16 transformation of the raw mesh. Next, the raw mesh is translated onto the template by
35
36 17 collocating the tip of the noses; the nose tip was identified in the raw mesh by assuming it to
37
38 18 be the maxima in the z -axis. Stage 3 utilises Iterative Closest Point (ICP) algorithm (Besl and
39
40 19 McKay, 1992) on the central facial area of the mesh (excluding ears, nose, neck) to rigidly
41
42 20 align the two meshes further. Finally, stage 4 employs Non-rigid Iterative Closest Point
43
44 21 algorithm (NICP) (Amberg et al., 2007) to morph the shape of the template mesh into the shape
45
46 22 of the aligned raw mesh, by incrementally moving each vertex on the template mesh closer to
47
48 23 their nearest neighbouring vertex on the aligned mesh.

49
50 24 The NICP is an essential step to bring all aligned meshes into dense correspondence with
51
52 25 one another. Figure 5 shows an example of dense correspondence achieved between 2 aligned
53
54 26 meshes: the shape of each aligned mesh was represented by a morphed template mesh or as
55
56 27 called a fitted mesh after NICP. These fitted mesh will have the same number of vertices
57
58 28 ($n=53,215$) and mesh structure as the template mesh. More importantly, every vertex on the
59
60 29 fitted mesh carries a consistent anatomical meaning. For example, the vertex at the tip of the
61
62 30 nose will always represent the tip of the nose, however its xyz coordinate values will change
63
64 31 across different fitted meshes.

32 2.3 Extract Region of Interest

1 Dense correspondence achieved in the previous step is critical for enabling the automatic
 2 identification and extraction of facial topographical data, or the Region of Interest (ROI) on the
 3 face. This is because individual vertices can now be used consistently as facial landmarks to
 4 identify area on the face that needs to be extracted. Without dense correspondence, this step
 5 can only be achieved via manual visual inspection. An algorithm was written in MATLAB to
 6 identify ROI on the face where the mask is expected to be in direct contact with the face. Details
 7 of the algorithm are explained as follow.

8 The ROI was determined by projecting a 2D egg shape parallel to the XY plane onto the
 9 3D surface of the fitted mesh, [Figure 6](#). A 2D parametric egg shape curve expressed in the
 10 following function was used to define the boundaries of the ROI:

$$x = ((c \times r) - (p \times r) \times \cos \theta) \times \sin \theta \quad (1)$$

$$y = r \times \cos \theta \quad (2)$$

13 where c is the circularity and p the pointiness of the egg shape. Together, c and p define the
 14 overall shape of the egg and their values were chosen as $c = 1$, and $p = 0.4$ such that the egg
 15 shape resembles the typical shape of commercially available respirator masks. The radius r
 16 determines the size of the egg. Two egg shapes were created with two radii to represent the
 17 outer and inner edge of the mask respectively. The [radius for the outer egg shape \(\$r_{outer}\$ \)](#) was
 18 defined as the y-axis distance between the philtrum and the lower edge of the chin for the outer
 19 edge, [Figure 6 \(a\)](#); and [the radius for the inner egg shape \(\$r_{inner}\$ \)](#) was 8 mm smaller ~~for the~~
 20 ~~inner edge~~, [Figure 6 \(b\)](#). The centre of the 2D egg was located at the philtrum xy coordinate
 21 and the z coordinate of the nose tip, [Figure 6 \(c\)](#). Vertices at the philtrum, chin and nose can be
 22 consistently identified across different faces because their indexing remain the same after the
 23 template fitting step, with only their xyz coordinates being altered. At this stage the 2D shape,
 24 size and location of the egg had been fully defined. Then, 100 points were evenly sampled on
 25 each egg shape and projected onto the fitted mesh surface. Their 3D coordinates were
 26 determined using a ray-triangle intersection operation. These projected points marked out the
 27 boundaries of ROI, shown as red and blue dots in [Figure 6 \(d\)](#) and referenced vertices as
 28 coloured asterisks.

2.4 Conceptual design and CAD API script

Figure 7 (a) shows the conceptual design of the respirator mask. The design was developed by taking into consideration of criteria outlined in international standards for respiratory protective devices and PPE (British Standards of BS EN 149-2001, and the European Union Regulation 2016/425), and taking inspirations from industrial half-mask respirators such as the 3M™ Half Facepiece Reusable Respirator 6200 (3M Company, Minnesota, USA) and popular design on open source CAD repository Thingiverse (lafactoria3d, 2020). The design of the mask was modularised to minimise the number of components that needs to be customised, while enabling easy disinfection, assembling and disassembling. It contains four components: *shell* (blue), *filter house* (green), *cap* (yellow) and *connector* (white). The *shell* is the main mask body, the *filter house* and *cap* secures an off-the-shelf filter material in place, and the *connector* is for straps.

All components were created parametrically in Autodesk Fusion 360. Parametric CAD models are built from successive addition of geometric entities (lines, curves etc.) and features (extrusion, revolve etc.) with defined rules and constraints (Saxena and Sahay, 2007). The geometry created later on in a modelling workflow is dependent on the geometry created earlier on. Therefore, given a carefully defined parametric CAD model, i.e. the dimensions for each entity and feature, and the geometric relations among them are fully defined, the final geometry of the CAD model can be easily modified by changing the values of a few parameters (e.g. dimensions). In this study, only the *shell* component will be in direct contact with the face, therefore its shape needed to be updated for each individual. The rest of the components are standardised, and their shapes remain unchanged for different individuals. To automatically update the shape of the *shell* component, a fully defined parametric model of the *shell* component was first manually created, then an API script was written to replicate the modelling workflow to achieve automation.

Essential modelling steps for creating the *shell* component are shown in Figure 7(b-e). ROI was first imported into Fusion 360 and fitted with two splines as shown in Figure 7(b). Then, the egg centre point extracted from the previous step was referenced as the centre to create a circular sketch for the filter, shown in Figure 7(c). A Boundary-Representation (BREP) surface was created by lofting from the bigger spline to the smaller spline then to the circular sketch to form the main body of the *shell*, as shown in Figure 7(d). This surface was the area on the mask that would be in direct contact with a face. Once a BREP surface was created, it was

1 thickened by 1.5mm to form a solid body. The filter part of the shell was created by extruding
2 the circular sketch away from the face by 10mm, and adding a thread on the inner surface of
3 the extrusion. Finally, fillets were added on the edges of the entire model to form the final *shell*
4 body, as shown in Figure 7 (e).

5 **2.4 Evaluations**

6 *2.4.1 Evaluate geometric accuracy of raw meshes*

7 Geometric accuracy of raw meshes for each volunteer were evaluated by calculating the
8 Hausdorff distance (Aspert et al., 2002) between raw meshes obtained from the 2D image, the
9 Light Stage, the Bellus3D app, and the ‘ground truth’ mesh obtained from the Artec Space
10 Spider. Meshes generated from the Artec were used as the ‘ground truth’ as it has the highest
11 reported 3D point accuracy, as well as the highest resolution (highest number of vertices per
12 unit area). Hausdorff distance is a commonly employed metric for comparing the distance
13 between two meshes in a 3D space. Its key advantage over a simple vertex to vertex Euclidean
14 distance metric is its robustness in comparing meshes of different structure, which is the case
15 in the present study.

16 Prior to carrying out the Hausdorff distance measurement, a few pre-processing steps were
17 carried out. Raw meshes were first automatically aligned to the ground truth mesh in MATLAB
18 using ICP algorithm that iteratively finds the optimal transformation matrix that best aligns a
19 raw mesh to the ground truth mesh. Then, the aligned mesh was imported into mesh processing
20 software Meshmixer (Autodesk, Inc., USA) to crop away noise and areas on the face that were
21 not present in the ground truth mesh (e.g. back of the head, neck, etc.). This was to ensure that
22 the maximum distance found between the two meshes would only be in the area that the two
23 meshes overlap.

24 Once the meshes were aligned and cropped, they were imported into another mesh
25 processing software MeshLab (MeshLab, 2020) and its in-built algorithm *Metro* (Cignoni et
26 al., 1998) was used to calculate the one-sided Hausdorff distance from the aligned mesh to the
27 ground truth. For each mesh, points on its vertices, edges, and faces were sampled (10 times
28 more than the number of vertices on the raw mesh) and the distance from the sampled point to
29 the closest point on the ground truth was measured. The computed distance values were saved
30 as a colour-coded 3D distance heat map where identical regions with a low distance value
31 between the two meshes were indicated in blue, areas in discrepancy were indicated in green,

1
2
3 1 yellow, and red with increasing distance value. The maximum of all distances for a single mesh,
4 and the average distance in root mean square (RMS) were recorded for each mesh.
5
6

7 8 3 *2.4.2 Evaluate geometric fitting of masks* 9

10 4 For each volunteer, raw facial meshes obtained from the 2D image, Light Stage and Bellus3D
11 were loaded into the custom-written MATLAB code to perform template fitting and extract
12 ROI using a MacBook Pro (3.5 GHz Intel Core i7, 16 GB 2133 MHz LPDDR3, Intel Iris Plus
13 Graphics 650 1536 MB). Once the ROI was extracted, it was inputted into the custom-written
14 Fusion API script to generate a customised CAD model of the mask on the same laptop.
15 Computational time needed to extract ROI in MATLAB and subsequent time needed to create
16 a mask in Fusion API was recorded respectively for each mesh.
17
18
19
20
21
22

23 11 For each volunteer, geometric deviations from the masks (obtained from 2D image, Light
24 Stage, and Bellus3D) to his/her corresponding ground truth facial mesh (obtained from the
25 Artec) were measured to determine how closely the mask can match the face. For each mask,
26 its surface that would be in direct contact with the face was first aligned to the ground truth in
27 MATLAB using ICP algorithm. Then, points were sampled on that surface and one-sided
28 Hausdorff distance was calculated from the mask to the ground truth in MeshLab. Similarly, a
29 colour-coded 3D distance heat map, the maximum distance and the RMS distance were
30 recorded for each mask.
31
32
33
34
35
36
37

38 19 *2.4.3 Prototyping* 39

40 20 Prototypes of the customised masks generated from Bellus3D meshes of the volunteers were
41 fabricated via a desktop SLA printer (Form2, Formlabs, USA). The masks were manufactured
42 from Formlabs Durable engineering resin (FLDUCL02, Formlabs, USA) using a layer height
43 of 0.1 mm. Durable resin has Polypropylene-like strength and stiffness properties, with a
44 postcured tensile modulus of 1 GPa and a flexural modulus of 0.66 GPa. Its soft and pliable
45 nature adds comfort to the user, whilst maintaining its mechanical strength and ensuring an
46 effective seal. To ensure the best surface finish for the mask sections in contact with skin, the
47 masks were printed in an orientation with the valve opening horizontal to the printing bed. This
48 ensured the support sections were always on the outer area of the mask. A support tip size of
49 0.4 mm was used to ensure surface defects were minimized, whilst ensuring a consistent print
50 quality. Once printed, the basic finishing steps for VAT polymerization were followed
51 (Redwood et al., 2017), including washing parts in IPA, drying and removal of supports before
52
53
54
55
56
57
58
59
60

1 curing. The parts were cured in a UV chamber for 60 minutes at 60 °C to reach their optimal
2 mechanical properties. Finally, areas where support was removed were sanded down to ensure
3 a smooth finish to the outer surface of the mask.

4 **3. Results and Discussion**

5 It is important to select an appropriate data acquisition method to ensure geometric accuracy of
6 the raw mesh while balancing time and cost required to carry out data acquisition quickly and
7 on a large scale in a pandemic crisis. The Hausdorff distance heat maps for facial meshes
8 generated from the various acquisition methods compared with the Artec ground truth mesh for
9 each volunteer are shown in Figure 8. The maximum and RMS distances are tabulated in Table
10 III. The facial mesh reconstructed by the LSFM from 2D images gave the largest geometric
11 discrepancy with RMS distances between 0.54 mm to 2.43 mm for the five volunteers, followed
12 by those from the Light Stage with RMS distances between 0.35 mm to 1.29 mm. Meshes
13 generated by the Bellus3D app using Apple TrueDepth camera gave the least geometric
14 discrepancy with RMS distances between 0.35 mm to 0.91 mm.

15 Figure 8 (a) shows the distance map between the mesh obtained from a 2D image and the
16 ground truth mesh obtained from the Artec Space Scanner for each volunteer. Large geometric
17 discrepancies were observed in different regions of the face: up to 1.85 mm at the forehead in
18 Volunteer 1, up to 8.55 mm on cheeks and chin of Volunteer 2, up to 3.58 mm on both sides of
19 the nose in Volunteer 3, up to 5.51 mm on the chin of Volunteer 4, and up to 3.79 mm on the
20 side of the nose in Volunteer 5. Large discrepancies were expected as data input was highly
21 deficient where there could be partial occlusion of the shape, variance in pose and lighting
22 conditions, and direct depth information was missing. Moreover, the reconstruction was
23 restricted by both the linearity of the LSFM model and its training data.

24 Distance heat maps from the Light Stage meshes are shown in Figure 8 (b). Facial mesh of
25 Volunteer 2 and 5 have the lowest geometric discrepancy in almost all regions of the face. The
26 largest discrepancies were observed at the eye and eyebrow regions as a result of poor
27 reconstruction for hair (eyebrows and eyelashes). Facial mesh of Volunteer 1, 3, and 4 had
28 various degrees of geometric discrepancy on the chin, forehead and right side of the cheek with
29 largest distance at 1.80 mm, 3.33 mm and 3.12 mm respectively. These discrepancies are likely
30 caused by missing direct depth information during the data acquisition process since only 2D
31 images with varying illumination conditions were used to infer depth information.

1
2
3 1 Facial data captured by the Apple TrueDepth camera produced the most geometrically
4 2 accurate facial reconstruction for all five participants, [Figure 8 \(c\)](#). The TrueDepth camera was
5 3 able to directly capture 3D depth information based on structured light principle (Salvi et al.,
6 4 2004), which is considered one of the most reliable techniques for recovering the surface of
7 5 objects. The regions on the face that gave the largest geometric discrepancies are at the eyes
8 6 and eyebrow regions where the presence of hair can greatly affect reconstruction results.
9 7 Nevertheless, these regions are outside the ROI of the mask, hence they will not affect the 'fit'
10 8 of the mask.

11
12
13
14
15
16
17
18 9 Choosing an appropriate data acquisition approach is the first crucial step towards
19 10 achieving mass customisation of a respirator mask. In a pandemic crisis, speed is essential for
20 11 delivering customised PPE to HCP, whilst travel restrictions and social distancing are practiced
21 12 globally. Given Table II, the fastest and most accessible data acquisition method among the
22 13 four tested acquisition methods would be the single 'in-the-wild' 2D image where anyone with
23 14 a phone equipped with a camera can do anywhere. However, results from [Figure 8 \(a\)](#) showed
24 15 that 3D reconstruction from a single 2D image can be highly unreliable for different faces. On
25 16 the other hand, reconstructions from the Bellus3D and Light Stage meshes were more accurate,
26 17 resulting in an average RMS distance less than 1 mm, as shown in Table III. While both
27 18 provided good geometric accuracy, it took only a few minutes by a volunteer to capture his
28 19 facial data using an iPhone X (£629) and the Bellus3D app (£0.55 per exported mesh), at any
29 20 location; while it took a specialist about half an hour to acquire the facial data of the same
30 21 volunteer using the Light Stage capturing system (costs between £50,000 - £100,000), at a
31 22 dedicated location. Clearly a phone equipped with a reliable depth sensor will be the most
32 23 practical data acquisition method in the midst of a pandemic, as it is fast, reliable, and does not
33 24 require additional manpower or cumbersome equipment. In this study, Apple TrueDepth
34 25 camera was employed as it was readily available among the authors of this paper. Other options
35 26 can also be explored such as the Samsung Galaxy S20 Ultra, Huawei P30 Pro, etc. While not
36 27 all phones came equipped with a depth camera now, as depth sensor technology matures, it is
37 28 likely that more and more phones will come with an in-built depth sensor in the future.

38
39
40
41
42
43
44
45
46
47
48
49
50
51
52
53
54 29 For each volunteer, regardless of the acquisition methods, a mask CAD model can be
55 30 successfully generated. For example, for volunteer 1, CAD model of the masks can be
56 31 successfully generated for facial mesh of volunteer 1 obtained through all four acquisition
57 32 methods. Since mesh generated from different acquisition methods differ by the number of
58
59
60

1
2
3 1 vertices and topologies, this demonstrated the robustness of our algorithm in handling meshes
4
5 2 with different mesh structures.
6
7

8 3 Geometric deviation of the mask surface to the volunteer's face were measured and
9
10 4 visualised as distance heat maps shown in Figure 9. All maximum and RMS distances were
11
12 5 tabulated in Table IV. By comparing the heat maps of the masks with that of the facial meshes,
13
14 6 it can be observed that geometric inaccuracies in facial meshes had been carried forward,
15
16 7 resulting in masks having similar geometric deviations at similar locations on the face. For
17
18 8 example, a large deviation of 8.55 mm was observed at the bridge of the nose in mask No.2,
19
20 9 shown in Figure 9(a); the same deviation was observed in the raw mesh generated from the 2D
21
22 10 image of Volunteer 2. This showed that our design process can accurately reconstruct the ROI
23
24 11 of a given facial mesh. How well a mask can fit onto its user depends largely on how accurate
25
26 12 the acquired raw 3D facial mesh is.

27
28 13 Time taken to perform template fitting and ROI extraction in MATLAB and generate a
29
30 14 customised CAD model in Fusion 360 were also tabulated in Table IV. Design time has been
31
32 15 significantly reduced as a result of automation. Time taken for MATLAB to process a raw mesh
33
34 16 generated from 2D image, Light Stage, Bellus3D and Artec was on average less than a minute
35
36 17 and half. Time taken to process the Artec mesh was almost doubled at an average of three
37
38 18 minutes and half. Longer time was needed because the Artec mesh consisted of an order of
39
40 19 magnitude more vertices than the other meshes, [which significantly slowed down the NICP](#)
41
42 20 [process](#). Time needed to generate a mask from Fusion script was much shorter at an average
43
44 21 6~7 seconds. Overall, our process took less than two minutes if the number of vertices in the
45
46 22 mesh is at ~50,000 (2D image and Light Stage) or ~100,000 (TrueDepth and Bellus3D). Even
47
48 23 with a large number of vertices at ~500,000 (Artec), the overall computational time was less
49
50 24 than four minutes per mask. This was a significant time saving as compared to those reported
51
52 25 in literature which can take hours from acquiring data to generating a custom-fitted CAD model
53
54 26 (Salles and Gyi, 2013a, Tuck et al., 2008). More importantly, further time reduction can be
55
56 27 achieved with greater processing power and/or more efficient algorithm. The only manual work
57
58 28 involved in this process was to trigger the MATLAB and Fusion scripts, which was done at the
59
60 29 click of a button. Such time and labour savings make it feasible for mass customising respirator
30
31 30 masks via AM as a quick response to equip HCP, who have failed the fit test, with a bespoke
32
33 31 mask that fits them. Additionally, to provide an alternative for frontline HCP who are suffering
34
35 32 from mask-related injuries due to prolonged usage and non-optimal fit.

1
2
3
4
5
6
7
8
9
10
11
12
13
14
15
16
17
18
19
20
21
22
23
24
25
26
27
28
29
30
31
32
33
34
35
36
37
38
39
40
41
42
43
44
45
46
47
48
49
50
51
52
53
54
55
56
57
58
59
60

1 All *shell* components of the mask generated from Bellus3D meshes successfully fabricated
2 are shown in Figure 10 (a). Significant differences in shapes and sizes can be observed in these
3 masks, due to the variation in facial shape and characteristic of each volunteer. On average it
4 took 8 hours and 40 mL of resin to fabricate a single *shell* component, and 4 hours and 25 mL
5 of resin to fabricate the three standard components (*connector*, *filter house*, *cap*). Figure 10 (b)
6 shows the complete concept respirator mask after assembling the four components. Figure 10
7 (c) shows one of the volunteers wearing his mask.

8 Overall, the proposed mass customisation design process can eliminate three manual tasks
9 needed in a conventional design customisation process to achieve automation, as shown in
10 Figure 11. Firstly, a raw facial mesh needs to be post-processed to remove holes and defects
11 caused by occlusions, movements during capture and the presence of hair. By fitting a raw
12 mesh to a template mesh, the fitted mesh will inherit the clean and complete mesh structure of
13 that template mesh. Hence, noise was minimised and holes were eliminated. Secondly, ROI on
14 the face needs to be identified and reverse engineered in a CAD environment to form a mask
15 surface that will be in direct contact with the face. It is challenging to identify ROI
16 automatically for different faces as there are few facial features that can be used consistently
17 across different faces as reference points. It is possible to make use of the RGB values in a
18 coloured mesh and leveraging on existing facial landmarking algorithms to identify key facial
19 features on a face for ROI extraction. However, variation in pose, lighting, facial expression,
20 and facial features can lead to significant errors in landmarking accuracy (Çeliktutan et al.,
21 2013, Johnston and de Chazal, 2018), therefore it remains a challenging approach. In this case,
22 a design engineer is still needed to conduct manual inspection on every facial mesh to identify
23 ROI. In our approach, a rigorous template fitting process via successive rigid and non-rigid
24 alignment steps was used to bring fitted meshes into dense correspondence, all vertices inherit
25 anatomical meaning of the template and can be used as reference landmarks, thereby making
26 the ROI identification and extraction process more reliable and robust across different faces.
27 Finally, the manual CAD modelling process was automated via API script as ROI were used
28 as parametric inputs to update the mask geometry. In the present study, a manual step is needed
29 to trigger the Fusion 360 API script, because Fusion 360 does not support external triggering.
30 Going forward, practitioners can explore other parametric CAD packages that can be readily
31 triggered externally to create a fully automated design pipeline.

1
2
3
4 1 While the study has introduced a novel and scalable design process that supports the MC
5 2 of 3D printed respirator masks to combat COVID-19 and future public health crises, concerted
6 3 efforts are still needed from policy makers, manufacturers, and the 3D printing community to
7 4 make MC of custom-fit 3D printed respirator masks a real alternative. A big hurdle to overcome
8 5 is the lack of specific regulatory guidance on the design and manufacture of 3D printed custom-
9 6 fit respirator mask, as evidenced by the lack of directives for 3D printed custom-fit PPE in the
10 7 European Union (EU) Regulation (EU) 2016/425. Even though the US Food and Drug
11 8 Administration has published Technical Considerations for Additive Manufactured Medical
12 9 Devices to guide the design and manufacture of 3D printed medical devices (Food and
13 10 Administration, 2017), and directed readers to the General Principles of Software Validation if
14 11 software were to be used for automating parts of an AM process (Food and Administration,
15 12 2002); there's no guidance specifically for PPE. Policy makers should look into the
16 13 development of detailed regulations specifically for the design and manufacture of 3D printed
17 14 PPE, including different sub-types of respirator masks (e.g. medical and non-medical), as the
18 15 certification processes for these respirator sub-types are different (Pecchia et al., 2020). Lessons
19 16 can be learnt from guidance for AM medical implants and orthotics, where process validation
20 17 has been emphasised for quality assurance. Apart from the lack of regulatory guidance,
21 18 manufacturers of respirator masks should work with designers, engineers and scientist to
22 19 conduct rigorous design iterations to select and incorporate an appropriate filter material to
23 20 ensure that the mask meets the filtering criteria of an N95 mask or equivalent. Appropriate
24 21 cleaning and disinfection protocols should also be developed considering the material
25 22 properties of the printed mask; lessons can be learnt from existing studies for re-usable
26 23 elastomeric half-mask respirators (Lawrence et al., 2017, Bessesen et al., 2015, Subhash et al.,
27 24 2014).

25 One limitation to the present study is the small sample size, which does not carry statistical
26 27 significance for a large population. Nevertheless, the facial characteristics of the five volunteers
28 28 are significantly different, mainly as a result of differences in age, gender and ethnicity (Table
29 29 I). Hence the results have demonstrated the potential of our method for handling different facial
30 30 shapes and characteristics. Future study is underway to recruit more number of participants to
31 31 obtain a larger sample size to further validate the process.

32 Another limitation to the study is the lack of quantitative or qualitative fit testing of the
33 32 fabricated masks to validate how well the physical prototype can fit onto its user. Nevertheless,
34 33

1
2
3 1 the Hausdorff distance heat maps have shown good results computationally. Future work
4
5 2 should be carried out to conduct more rigorous fit testing, such as Quantitative Fit Testing and
6
7 3 Qualitative Fit testing to evaluate the printed masks.
8

9 4 **4. Conclusion**

10 5 We have proposed a novel and scalable design process for the mass customisation of 3D printed
11
12 6 respirator masks to combat COVID-19. Four different data acquisition methods were evaluated
13
14 7 against geometric accuracies, cost and time considerations, where the one using a smart phone
15
16 8 depth sensor was deemed the most appropriate for MC of respirator mask in a pandemic crisis.
17
18 9 Subsequently, a three-step design process was proposed and scripted to enable automatic
19
20 10 generation of a custom-fit respirator mask CAD model from the input of a raw 3D facial mesh,
21
22 11 which took on average a minute and half for one mask. These results have implied that the new
23
24 12 design process is a promising route towards future respirator mask and PPE mass customisation
25
26 13 in a more time- and cost-efficient manner.
27
28
29
30
31
32
33
34
35
36
37
38
39
40
41
42
43
44
45
46
47
48
49
50
51
52
53
54
55
56
57
58
59
60

1 References

- 2 *Transcript for the OSHA Training Video Entitled Respirator Fit Testing* [Online]. Occupational Safety
3 and Health Administration. Available:
4 https://www.osha.gov/video/respiratory_protection/fittesting_transcript.html [Accessed
5 August 29th 2020].
- 6 AMBERG, B., ROMDHANI, S. & VETTER, T. Optimal step nonrigid ICP algorithms for surface
7 registration. 2007 IEEE Conference on Computer Vision and Pattern Recognition, 2007. IEEE,
8 1-8.
- 9 ASPERT, N., SANTA-CRUZ, D. & EBRAHIMI, T. Mesh: Measuring errors between surfaces using the
10 hausdorff distance. Proceedings. IEEE international conference on multimedia and expo,
11 2002. IEEE, 705-708.
- 12 BESL, P. J. & MCKAY, N. D. Method for registration of 3-D shapes. Sensor fusion IV: control
13 paradigms and data structures, 1992. International Society for Optics and Photonics, 586-
14 606.
- 15 BESSESEN, M. T., ADAMS, J. C., RADONOVICH, L., et al. 2015. Disinfection of reusable elastomeric
16 respirators by health care workers: a feasibility study and development of standard
17 operating procedures. *American journal of infection control*, 43, 629-634.
- 18 BLANZ, V. & VETTER, T. A morphable model for the synthesis of 3D faces. Proceedings of the 26th
19 annual conference on Computer graphics and interactive techniques, 1999. 187-194.
- 20 BOOTH, J., ROUSSOS, A., PONNIAH, A., et al. 2018. Large scale 3D morphable models. *International
21 Journal of Computer Vision*, 126, 233-254.
- 22 CAVALLO, L., MARCIANÒ, A., CICCÌ, M., et al. 2020. 3D printing beyond dentistry during COVID 19
23 epidemic: A technical note for producing connectors to breathing devices. *Prosthesis*, 2, 46-
24 52.
- 25 CAZON, A., AIZPURUA, J., PATERSON, A., et al. 2014. Customised design and manufacture of
26 protective face masks combining a practitioner-friendly modelling approach and low-cost
27 devices for digitising and additive manufacturing: This paper analyses the viability of
28 replacing conventional practice with AM method to make customized protective face masks.
29 *Virtual and Physical Prototyping*, 9, 251-261.
- 30 CELIK, H. K., KOSE, O., ULMEANU, M.-E., et al. 2020. Design and Additive Manufacturing of Medical
31 Face Shield for Healthcare Workers Battling Coronavirus (COVID-19). *International journal of
32 bioprinting*, 6.
- 33 ÇELIKTUTAN, O., ULUKAYA, S. & SANKUR, B. 2013. A comparative study of face landmarking
34 techniques. *EURASIP Journal on Image and Video Processing*, 2013, 13.
- 35 CHENG, Y. L. & CHU, J. C. 2013. Application of rapid tooling to manufacture customized nasal mask
36 cushion for continuous positive airway pressure (CPAP) devices. *Rapid Prototyping Journal*.
- 37 CHU, C.-H., HUANG, S.-H., YANG, C.-K., et al. 2015. Design customization of respiratory mask based
38 on 3D face anthropometric data. *International Journal of Precision Engineering and
39 Manufacturing*, 16, 487-494.
- 40 CHU, C.-H., WANG, I.-J., WANG, J.-B., et al. 2017. 3D parametric human face modeling for
41 personalized product design: Eyeglasses frame design case. *Advanced Engineering
42 Informatics*, 32, 202-223.
- 43 CIGNONI, P., ROCCHINI, C. & SCOPIGNO, R. Metro: measuring error on simplified surfaces. Computer
44 graphics forum, 1998. Wiley Online Library, 167-174.
- 45 CLIFTON, W., DAMON, A. & MARTIN, A. K. 2020. Considerations and Cautions for Three-Dimensional-
46 Printed Personal Protective Equipment in the COVID-19 Crisis. *3D Printing and Additive
47 Manufacturing*.
- 48 DA SILVEIRA, G., BORENSTEIN, D. & FOGLIATTO, F. S. 2001. Mass customization: Literature review
49 and research directions. *International journal of production economics*, 72, 1-13.

- 1
2
3 1 DEBEVEC, P. 2012. The light stages and their applications to photoreal digital actors. *SIGGRAPH Asia*,
4 2 2.
5 3 FLANAGAN, S. T. & BALLARD, D. H. 2020. 3D Printed Face Shields: A Community Response to the
6 4 COVID-19 Global Pandemic. *Academic Radiology*, 27, 905.
7 5 FOGLIATTO, F. S., DA SILVEIRA, G. J. & BORENSTEIN, D. 2012. The mass customization decade: An
8 6 updated review of the literature. *International Journal of production economics*, 138, 14-25.
9 7 FOOD, U. & ADMINISTRATION, D. 2002. General principles of software validation: Final guidance for
10 8 industry and FDA staff. *Center for Devices and Radiological Health, Tech. Rep.*
11 9 FOOD, U. & ADMINISTRATION, D. 2017. Technical Considerations for Additive Manufactured Medical
12 10 Devices. *Guidance for Industry and Food and Drug Administration Staff.*
13 11 GATES, B. 2020. Responding to Covid-19—a once-in-a-century pandemic? *New England Journal of*
14 12 *Medicine*, 382, 1677-1679.
15 13 GEFEN, A., ALVES, P., CIPRANDI, G., et al. 2020. Device-related pressure ulcers: SECURE prevention.
16 14 *Journal of wound care*, 29, S1-S52.
17 15 GHOSH, A., FYFFE, G., TUNWATTANAPONG, B., et al. Multiview face capture using polarized spherical
18 16 gradient illumination. *Proceedings of the 2011 SIGGRAPH Asia Conference*, 2011. 1-10.
19 17 GREIG, P., CARVALHO, C., EL-BOGHDADLY, K., et al. 2020. Safety testing improvised COVID-19
20 18 personal protective equipment based on a modified full-face snorkel mask. *Anaesthesia*.
21 19 HSIAO, H. 2013. Anthropometric procedures for protective equipment sizing and design. *Human*
22 20 *factors*, 55, 6-35.
23 21 JOHNSTON, B. & DE CHAZAL, P. 2018. A review of image-based automatic facial landmark
24 22 identification techniques. *EURASIP Journal on Image and Video Processing*, 2018, 86.
25 23 KAMPOURIS, C. & GHOSH, A. ICL multispectral light stage: building a versatile LED sphere with off-
26 24 the-shelf components. *Proceedings of the Eurographics 2018 Workshop on Material*
27 25 *Appearance Modeling*, 2018. Eurographics Association, 1-4.
28 26 KAMPOURIS, C., ZAFEIRIOU, S. & GHOSH, A. Diffuse-Specular Separation using Binary Spherical
29 27 Gradient Illumination. *EGSR (EI&I)*, 2018. 1-10.
30 28 LACKO, D., HUYSMANS, T., VLEUGELS, J., et al. 2017. Product sizing with 3D anthropometry and k-
31 29 medoids clustering. *Computer-Aided Design*, 91, 60-74.
32 30 LAFACTORIA3D. 2020. *COVID-19 MASK v2 (Fast print, no support, filter required)* [Online].
33 31 Thingiverse. Available: <https://www.thingiverse.com/thing:4225667> [Accessed May 2020].
34 32 LAN, J., SONG, Z., MIAO, X., et al. 2020. Skin damage among health care workers managing
35 33 coronavirus disease-2019. *Journal of the American Academy of Dermatology*, 82, 1215-1216.
36 34 LATTAS, A., WANG, M., ZAFEIRIOU, S., et al. 2019. Multi-view facial capture using binary spherical
37 35 gradient illumination. *ACM SIGGRAPH 2019 Posters*.
38 36 LAWRENCE, C., HARNISH, D. A., SANDOVAL-POWERS, M., et al. 2017. Assessment of half-mask
39 37 elastomeric respirator and powered air-purifying respirator reprocessing for an influenza
40 38 pandemic. *American journal of infection control*, 45, 1324-1330.
41 39 MESHLAB. 2020. *MeshLab* [Online]. Available: <https://www.meshlab.net/> [Accessed December
42 40 2020].
43 41 NOVAK, J. I. & LOY, J. 2020a. A critical review of initial 3D printed products responding to COVID-19
44 42 health and supply chain challenges. *Emerald Open Research*, 2, 24.
45 43 NOVAK, J. I. & LOY, J. 2020b. A quantitative analysis of 3D printed face shields and masks during
46 44 COVID-19. *Emerald Open Research*, 2.
47 45 PALLARI, J. H., DALGARNO, K. W. & WOODBURN, J. 2010. Mass customization of foot orthoses for
48 46 rheumatoid arthritis using selective laser sintering. *IEEE Transactions on Biomedical*
49 47 *Engineering*, 57, 1750-1756.
50 48 PATERSON, A. M., DONNISON, E., BIBB, R. J., et al. 2014. Computer-aided design to support
51 49 fabrication of wrist splints using 3D printing: A feasibility study. *Hand Therapy*, 19, 102-113.
52
53
54
55
56
57
58
59
60

- 1
2
3 1 PECCHIA, L., PIAGGIO, D., MACCARO, A., et al. 2020. The Inadequacy of Regulatory Frameworks in
4 2 Time of Crisis and in Low-Resource Settings: Personal Protective Equipment and COVID-19.
5 3 *Health and Technology*, 1.
6 4 POMPEII, L. A., KRAFT, C. S., BROWNSWORD, E. A., et al. 2020. Training and fit testing of health care
7 5 personnel for reusable elastomeric half-mask respirators compared with disposable N95
8 6 respirators. *Jama*, 323, 1849-1852 %@ 0098-7484.
9 7 PROVENZANO, D., RAO, Y. J., MITIC, K., et al. 2020. Rapid prototyping of reusable 3D-printed N95
10 8 equivalent respirators at the George Washington University.
11 9 REDWOOD, B., SCHFFER, F. & GARRET, B. 2017. *The 3D printing handbook: technologies, design and*
12 10 *applications*, 3D Hubs.
13 11 ROGERS, B., BOSKER, G. W., CRAWFORD, R. H., et al. 2007. Advanced trans-tibial socket fabrication
14 12 using selective laser sintering. *Prosthetics and orthotics international*, 31, 88-100.
15 13 SAGONAS, C., TZIMIROPOULOS, G., ZAFEIRIOU, S., et al. A semi-automatic methodology for facial
16 14 landmark annotation. Proceedings of the IEEE conference on computer vision and pattern
17 15 recognition workshops, 2013. 896-903.
18 16 SALLES, A. S. & GYI, D. E. 2012. The specification of personalised insoles using additive
19 17 manufacturing. *Work*, 41, 1771-1774.
20 18 SALLES, A. S. & GYI, D. E. 2013a. Delivering personalised insoles to the high street using additive
21 19 manufacturing. *International Journal of Computer Integrated Manufacturing*, 26, 386-400.
22 20 SALLES, A. S. & GYI, D. E. 2013b. An evaluation of personalised insoles developed using additive
23 21 manufacturing. *Journal of Sports Sciences*, 31, 442-450.
24 22 SALVI, J., PAGES, J. & BATLLE, J. 2004. Pattern codification strategies in structured light systems.
25 23 *Pattern recognition*, 37, 827-849.
26 24 SAXENA, A. & SAHAY, B. 2007. *Computer aided engineering design*, Springer Science & Business
27 25 Media.
28 26 SCHONBERGER, J. L. & FRAHM, J.-M. Structure-from-motion revisited. Proceedings of the IEEE
29 27 Conference on Computer Vision and Pattern Recognition, 2016. 4104-4113.
30 28 SCHÖNBERGER, J. L., ZHENG, E., FRAHM, J.-M., et al. Pixelwise view selection for unstructured multi-
31 29 view stereo. European Conference on Computer Vision, 2016. Springer, 501-518.
32 30 SCHRANK, E. S. 2011. Dimensional accuracy of ankle-foot orthoses constructed by rapid
33 31 customization and manufacturing framework. *Journal of rehabilitation research and*
34 32 *development*, 48, 31.
35 33 SPALLEK, J. & KRAUSE, D. 2016. Process types of customisation and personalisation in design for
36 34 additive manufacturing applied to vascular models. *Procedia CIRP*, 50, 281-286.
37 35 SUBHASH, S. S., CAVAIUOLO, M., RADONOVICH, L. J., et al. 2014. Effectiveness of Common
38 36 Healthcare Disinfectants against H1N1 Influenza Virus on Reusable Elastomeric Respirators.
39 37 *Infection Control & Hospital Epidemiology*, 35, 894-897.
40 38 SWENNEN, G. R., POTTEL, L. & HAERS, P. E. 2020. Custom-made 3D-printed face masks in case of
41 39 pandemic crisis situations with a lack of commercially available FFP2/3 masks. *International*
42 40 *Journal of Oral and Maxillofacial Surgery*.
43 41 TUCK, C. J., HAGUE, R. J., RUFFO, M., et al. 2008. Rapid manufacturing facilitated customization.
44 42 *International Journal of Computer Integrated Manufacturing*, 21, 245-258.
45 43 UNAL, G., NAIN, D., SLABAUGH, G., et al. Customized design of hearing aids using statistical shape
46 44 learning. International Conference on Medical Image Computing and Computer-Assisted
47 45 Intervention, 2008. Springer, 518-526.
48 46 VERWULGEN, S., LACKO, D., VLEUGELS, J., et al. 2018. A new data structure and workflow for using
49 47 3D anthropometry in the design of wearable products. *International Journal of Industrial*
50 48 *Ergonomics*, 64, 108-117.
51 49 WESEMANN, C., PIERALLI, S., FRETWURST, T., et al. 2020. 3-d printed protective equipment during
52 50 covid-19 pandemic. *Materials*, 13, 1997.
53
54
55
56
57
58
59
60

1
2
3
4
5
6
7
8
9
10
11
12
13
14
15
16
17
18
19
20
21
22
23
24
25
26
27
28
29
30
31
32
33
34
35
36
37
38
39
40
41
42
43
44
45
46
47
48
49
50
51
52
53
54
55
56
57
58
59
60

1 WHO 2020. Advice on the use of masks in the context of COVID-19: interim guidance, 5 June 2020.
2 World Health Organization.
3 WILKINSON, I. J., PISANIELLO, D., AHMAD, J., et al. 2010. Evaluation of a large-scale quantitative
4 respirator-fit testing program for healthcare workers: survey results. *infection control and*
5 *hospital epidemiology*, 31, 918.
6 YU, Y., JIANG, L., ZHUANG, Z., et al. 2014. Fitting characteristics of N95 filtering-facepiece respirators
7 used widely in China. *PLoS One*, 9, e85299.

Rapid Prototyping Journal

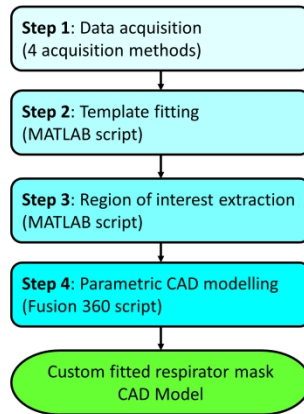


Figure 1. Data flow from collection to CAD processing for each volunteer.

338x190mm (300 x 300 DPI)

1
2
3
4
5
6
7
8
9
10
11
12
13
14
15
16
17
18
19
20
21
22
23
24
25
26
27
28
29
30
31
32
33
34
35
36
37
38
39
40
41
42
43
44
45
46
47
48
49
50
51
52
53
54
55
56
57
58
59
60

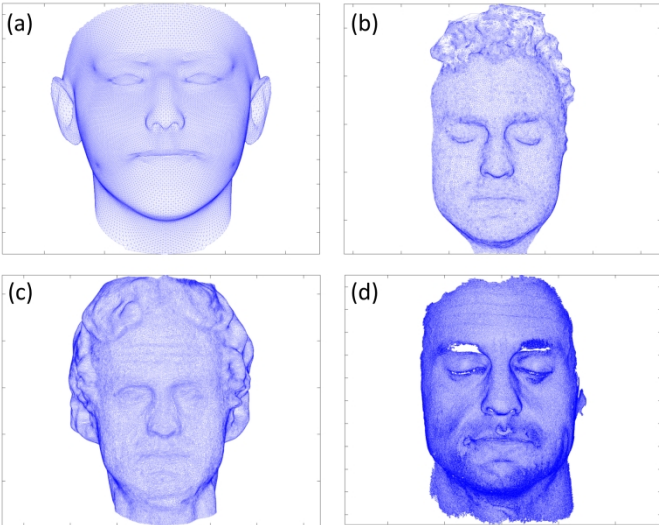


Figure 2. 3D facial mesh obtained via various acquisition methods. (a) LSMF reconstruction from a 2D image, (b) Light Stage, (c) Bellus3D using Apple TrueDepth camera, (d) Artec Space Spider.

338x190mm (300 x 300 DPI)

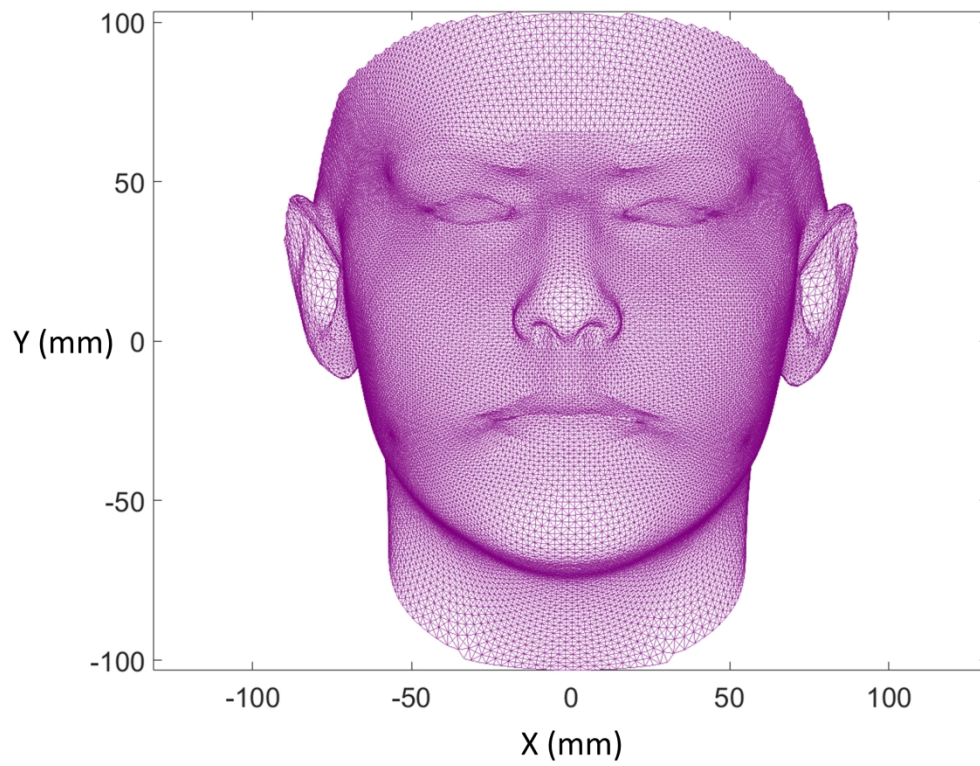


Figure 3. Universal template facial mesh.

1
2
3
4
5
6
7
8
9
10
11
12
13
14
15
16
17
18
19
20
21
22
23
24
25
26
27
28
29
30
31
32
33
34
35
36
37
38
39
40
41
42
43
44
45
46
47
48
49
50
51
52
53
54
55
56
57
58
59
60

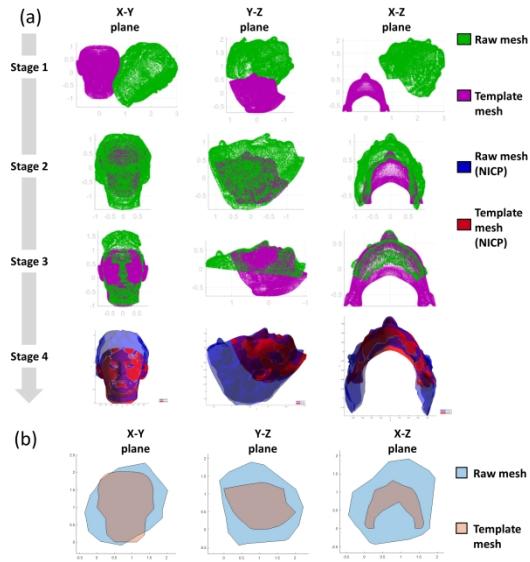


Figure 4. Template fitting process. (a) four stages of template fitting: 1. pre-processing, 2. coarse rigid alignment, 3. fine rigid alignment, and 4. non-rigid alignment stage, (b) error minimization in coarse alignment stage 2.

338x190mm (300 x 300 DPI)

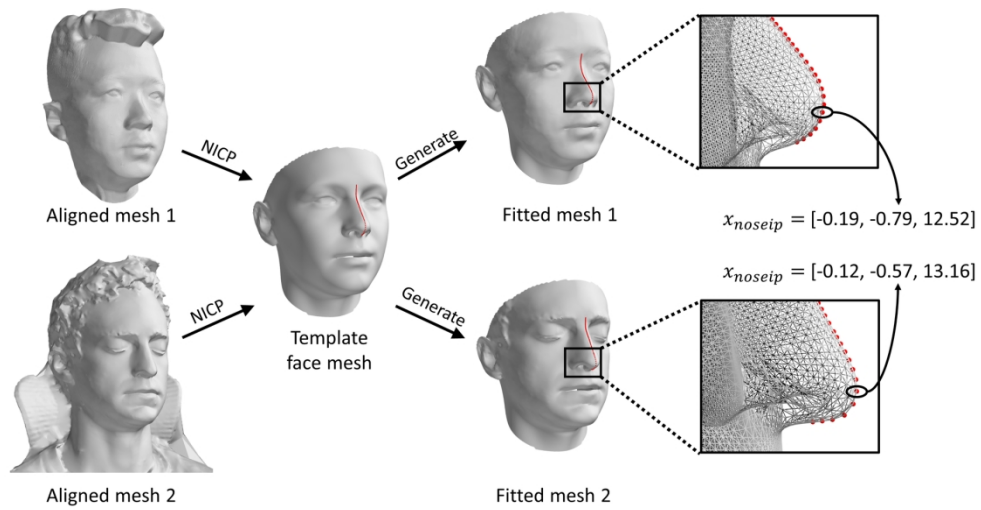


Figure 5. Create dense correspondence via NICP algorithm.

338x190mm (150 x 150 DPI)

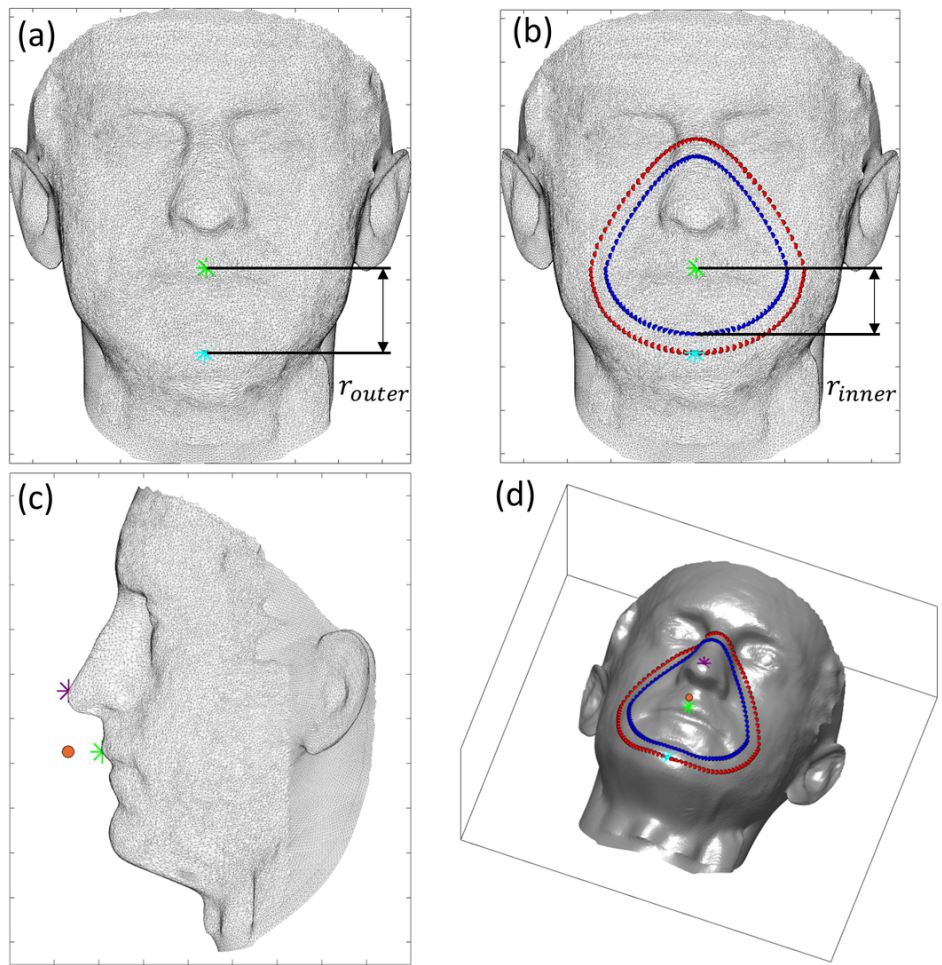


Figure 6. Extract ROI. (a) Philtrum vertex (green) and Chin vertex (cyan) shown in the XY plane, (b) inner (blue) and outer (red) mask edge points, (c) Philtrum vertex (green), Nose tip vertex (purple) and centre location (orange) shown in the YZ plane, (d) 3D view of referenced vertices (asterisks) and extracted data (dots).

190x190mm (150 x 150 DPI)

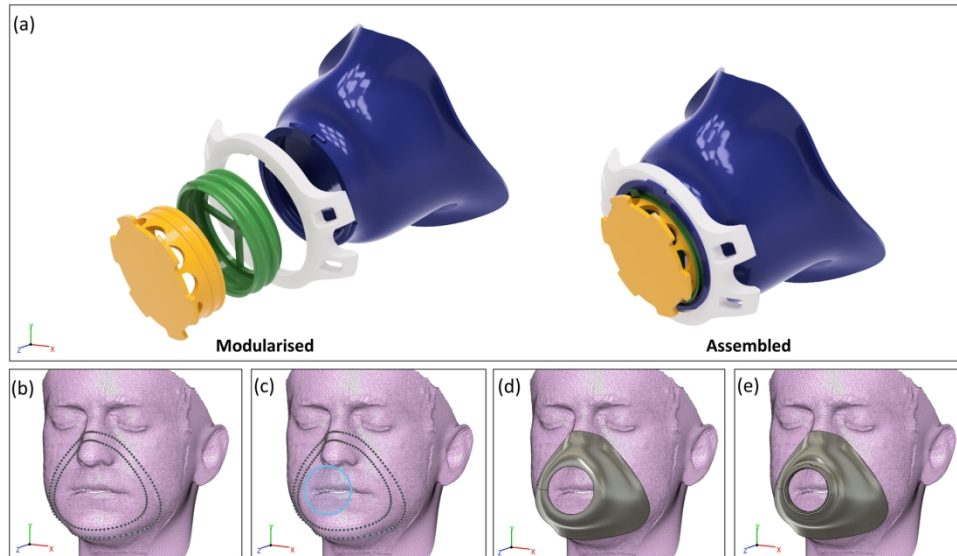


Figure 7. Mask conceptual design and CAD modelling workflow. (a) mask being modularised into four components, (b) splines fitted to ROI, (c) egg centre point used to create the sketch for filter house, (d) loft to create the entire mask body, (e) the final shell design.

338x190mm (150 x 150 DPI)

1
2
3
4
5
6
7
8
9
10
11
12
13
14
15
16
17
18
19
20
21
22
23
24
25
26
27
28
29
30
31
32
33
34
35
36
37
38
39
40
41
42
43
44
45
46
47
48
49
50
51
52
53
54
55
56
57
58
59
60

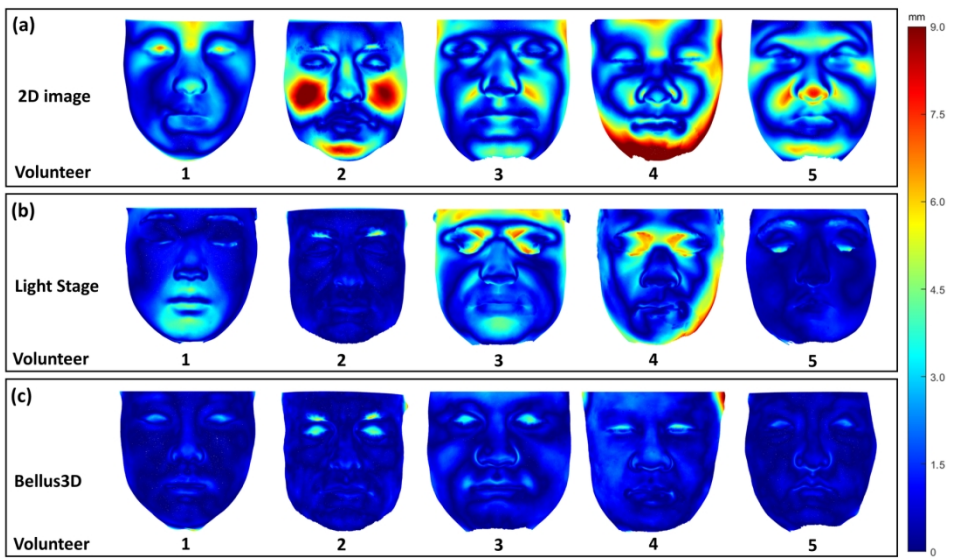


Figure 8. Hausdorff distance heat maps of raw meshes compared with Artec ground truth mesh for Volunteer 1-5. For meshes generated by (a) LSFM from a 2D image, (b) Light Stage, (c) the Bellus3D app.

338x190mm (150 x 150 DPI)

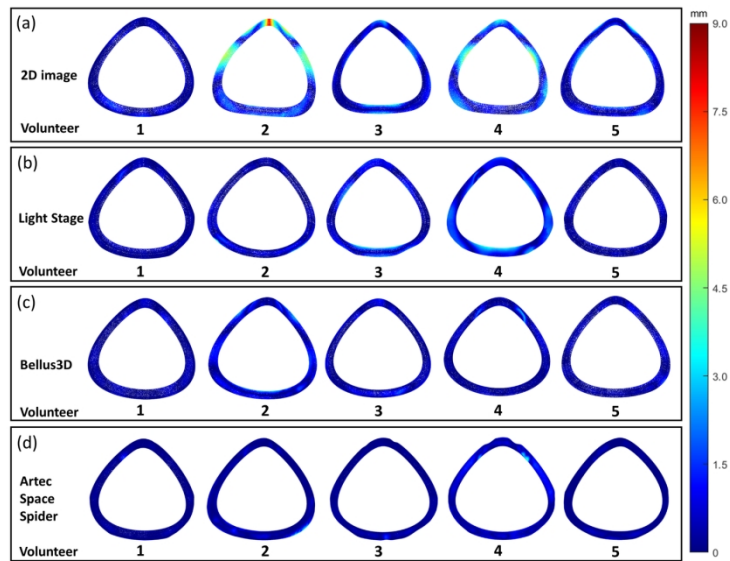


Figure 9. Distance heat maps of mask surface compared with Artec ground truth mesh for Volunteer 1-5. For masks generated from (a) 2D image mesh, (b) Light Stage mesh, (c) Bellus3D mesh, (d) Artec mesh.

338x190mm (150 x 150 DPI)

1
2
3
4
5
6
7
8
9
10
11
12
13
14
15
16
17
18
19
20
21
22
23
24
25
26
27
28
29
30
31
32
33
34
35
36
37
38
39
40
41
42
43
44
45
46
47
48
49
50
51
52
53
54
55
56
57
58
59
60

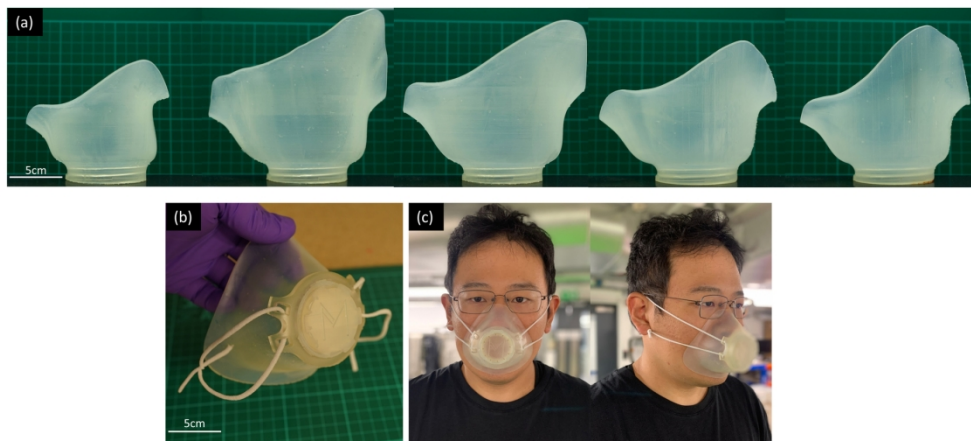


Figure 10. Masks fabricated via an SLA printer. (a) from left to right: customised mask for volunteer 1 to 5, (b) an example of a mask assembly, (c) A volunteer wearing his custom-fit respirator mask.

338x170mm (150 x 150 DPI)

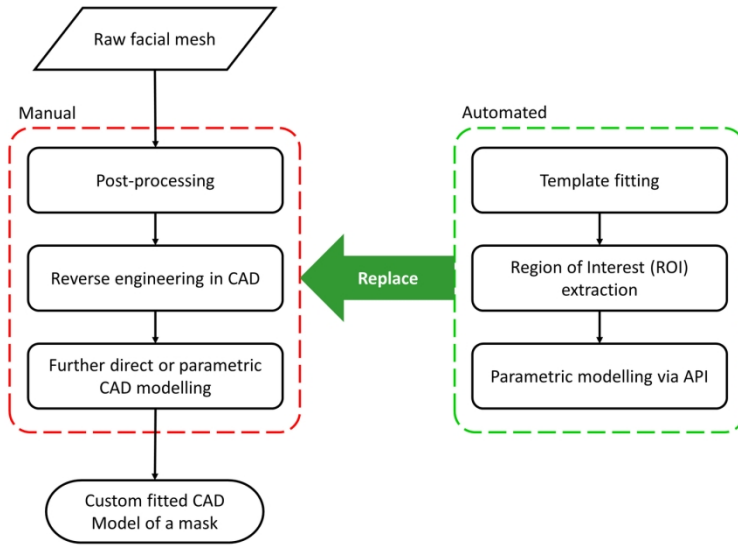


Figure 11. Conventional design process (left) compared with proposed mass customisation design process (right).

338x190mm (150 x 150 DPI)

1
2
3
4
5
6
7
8
9
10
11
12
13
14
15
16
17
18
19
20
21
22
23
24
25
26
27
28
29
30
31
32
33
34
35
36
37
38
39
40
41
42
43
44
45
46

Table I. Demographics of all volunteers

Volunteer	Age	Gender	Height (cm)	Weight (kg)	Body Mass Index (kg/m²)	Ethnicity
1	27	Female	158	50	20.03	Asian, Chinese;
2	35	Male	183	76	22.69	White, English / Welsh / Scottish / Northern Irish / British;
3	27	Male	181	85	25.95	White, Any other White background;
4	32	Male	178	100	31.56	Asian, any other Asian background;
5	26	Male	171	63	21.55	Asian, any other Asian background;

Rapid Prototyping Journal

Table II. Details of the four acquisition methods

Acquisition method	Equipment	Equipment parameters	Equipment cost	Acquisition Time (minute)	Software/ Algorithm	Software cost	File format	File size	Number of vertices
RECONSTRUCTION FROM A 2D IMAGE USING A MORPHABLE MODEL	Iphone 6s, back-facing camera	12 megapixel, f/2.2 aperture	£249	< 1 minute	Large-scale Statistical Face Model	Free	OBJ	~5MB	53,215
PHOTOMETRIC-STEREO RECONSTRUCTION	Imperial College Multispectral Light Stage: - 336 white and RGB Philips Colour Kinetics - 9 Canon EOS800D	9x 24megapixel (portrait) DSLR cameras combined into 1x 24 megapixel (landscape), 3fps capturing speed, f/11, ISO 200	£50,000~ £100,000	10~15 minutes	COLMAP, MeshLab	Free	OBJ	~5MB	Up to 50,000
RGB + DEPTH VIDEO SEQUENCE	Apple Iphone X TrueDepth camera	7 megapixel, f/2.2 aperture, backside illumination sensor, Retina Flash	£629	1~2 minutes	Bellus3D app Artec Studio 11	£0.55/exported mesh	OBJ	~10MB	~100,000
STRUCTURED-LIGHT	Artec 3D Space Spider handheld scanner	Geometry tracking mode, 15 fps scanning speed	£18,641	20~30 minutes	Artec Studio 11 Professional software	Free	OBJ	~50MB	~500,000

Table III. Geometric discrepancy between a raw mesh and the Artec ground truth mesh

Volunteer	Maximum distance (mm)			RMS distance (mm)		
	2D Image	Light Stage	Bellus3D	2D Image	Light Stage	Bellus3D
1	1.85	1.80	1.41	0.54	0.35	0.35
2	8.55	5.31	2.86	2.43	0.72	0.91
3	3.58	3.33	1.86	1.03	1.02	0.55
4	5.51	3.12	3.00	1.76	1.29	0.55
5	3.79	1.29	1.79	1.01	0.37	0.46
Average	4.66	2.97	2.18	1.35	0.75	0.56

Table IV. Computational time and geometric accuracy of the masks

Volunteer	Time for MATLAB (min:sec)				Time for Fusion (min:sec)			
	2D Image	Light Stage	Bellus3D	Artec	2D Image	Light Stage	Bellus3D	Artec
1	01:17	01:21	01:27	03:34	00:07	00:07	00:06	00:07
2	01:18	01:20	01:41	03:43	00:06	00:07	00:07	00:07
3	01:21	01:22	01:27	03:24	00:06	00:07	00:06	00:06
4	01:16	01:17	01:26	03:30	00:07	00:07	00:06	00:07
5	01:20	01:22	01:21	03:05	00:06	00:07	00:06	00:06
Average	01:18	01:20	01:28	03:27	00:06	00:06	00:06	00:07
Volunteer	Maximum distance (mm)				RMS distance (mm)			
	2D Image	Light Stage	Bellus3D	Artec	2D Image	Light Stage	Bellus3D	Artec
1	1.85	1.80	1.41	1.58	0.54	0.35	0.35	0.18
2	8.55	5.31	2.86	3.36	2.43	0.72	0.91	0.49
3	3.58	3.33	1.86	1.63	1.03	1.02	0.55	0.27
4	5.51	3.12	3.00	2.80	1.76	1.29	0.55	0.35
5	3.79	1.29	1.79	1.66	1.01	0.37	0.46	0.21
Average	4.66	2.97	2.18	2.21	1.35	0.75	0.56	0.30